The effect of deep brain stimulation on cortico-subcortical networks in Parkinson's disease patients with freezing of gait: Exhaustive exploration of a basic model

Mariia Popova[1*], Arnaud Messé[1], Alessandro Gulberti[2], Christian Gerloff[2], Monika Pötter-Nerger[2], Claus C Hilgetag[1]

1 Institute of Computational Neuroscience, Hamburg Center of Neuroscience, University Medical Center Hamburg-Eppendorf, Hamburg University, Hamburg, Germany
2 Department of Neurology, Hamburg Center of Neuroscience, University Medical Center Hamburg-Eppendorf, Hamburg University, Hamburg, Germany

* m.popova@uke.de

Abstract

Current treatments of Parkinson's disease (PD) have limited efficacy in alleviating axial symptoms, such as freezing of gait (FoG). In this context, concomitant deep brain stimulation (DBS) of the subthalamic nucleus (STN) and the substantia nigra pars reticulata (SNr) has been suggested as a potential therapeutic approach. However, the mechanism underlying this paired stimulation approach is unknown. The hypothetical rationale behind it relies on network-based hypotheses of intensified disinhibition of brainstem locomotor areas to facilitate the release of gait motor programs. However, to date, it is unclear how simultaneous high-frequency DBS in two different interconnected basal ganglia nuclei affect large-scale cortico-subcortical network activity. Here, we use a basic model of neural excitation, the susceptible-excited-refractory (SER) model, to compare the effects of different stimulation modes on the cortico-subcortical network underlying FoG. We develop a new network-based computational framework to uncover the most effective subcortical DBS target sites and their combinations through exhaustive analysis of the brain attractor dynamics in the healthy, PD and DBS states. We demonstrate the validity of the approach and the superior performance of combined STN+SNr DBS in the normalization of spike propagation flow in the FoG network. The present framework aims to move towards a better mechanistic understanding of the brain network effects of DBS and may be applicable to further perturbation-based therapies of brain disorders.

Author summary

Parkinson's disease patients with freezing of gait may be treated by deep brain stimulation, which has local as well as long-range effects that are mediated by brain networks. Currently, the approach of combined DBS of the subthalamic nucleus and the substantia nigra pars reticulata is investigated for being especially beneficial for patients with axial symptoms, but the exact mechanisms for this effect remain unknown. Here, we present a network-based computational framework using a basic excitable model that enables us to simulate the complete activity patterns of the brain network involved in FoG. These simulations unravel the mechanisms behind STN+SNr DBS and its efficacy in alleviating FoG. The proposed framework can capture the influence of the DBS

target sites on cortico-subcortical networks and help to identify suitable stimulation target regions.

Introduction

Parkinson's disease is a progressive neurodegenerative disorder with cardinal motor symptoms such as axial and limb bradykinesia, rest tremor, and rigidity [1]. Many PD symptoms are successfully treated pharmacologically [2] or by deep brain stimulation [3, 4]. However, axial symptoms, such as parkinsonian gait disorder, postural instability and freezing of gait show limited response to treatment [5, 6]. FoG is associated with an increased risk of falls among the patients and represents a significant source of morbidity. Thus, there is a need to reconcile FoG network pathophysiology and efficient treatment approaches.

DBS is an established treatment strategy for PD patients with motor fluctuations, medically refractory tremor or severe dopaminergic drug reactions [7]. Despite wide use of DBS in the clinical routine, the mechanism of its action remains poorly understood. DBS efficacy varies largely between patients, and particularly gait disorders and FoG appear to respond better to specific stimulation patterns [5]. It was recently shown that simultaneous deep brain stimulation of STN and SNr (STN+SNr DBS) outperforms standard STN DBS in improving FoG symptoms [8–10]. However, there is a possibility of worsening akinesia [8], hypomania [11], mania [12], and depression [13] with SNr stimulation, partly due to projections of the SNr to the limbic system [5]. Therefore, while it is an attractive alternative to induce co-stimulation of SNr with STN when treating patients with DBS-resistant FoG, it is essential to assess and understand its mechanistic effect on cortico-subcortical networks.

The effects of DBS are thought to rely not only on the specific properties of individual neurons, but on the properties of large-scale brain networks [14]. The STN+SNr DBS efficacy in alleviating FoG is based on the notion that gait disturbances during advanced PD are associated with defective motor processing in the mesencephalic locomotor region (MLR) [15]. MLR is densely interconnected with SNr, a major output nucleus in the basal ganglia. Thus, a faulty output of the basal ganglia system in PD might result in over-inhibition of MLR due to GABAergic projections of the SNr and subsequent attenuation of locomotor activity [16]. In turn, functional inhibition of STN and SNr due to DBS [17] is likely to attenuate over-inhibitory SNr output and lead to restored gait and posture. To study the DBS network effects, we represent a cortico-subcortical network of regions involved in FoG episode generation as a directed signed graph. The network includes the basal ganglia and brainstem regions as nodes, and the excitatory or inhibitory synaptic connections as signed edges. The graph representation of the FoG network facilitates examining its topological properties, and allows in-silico simulations of neural activity.

Our present goal is to introduce a mathematical framework that explains possible differences in the activity propagation along the cortico-subcortical projections due to the chosen DBS target (Fig. 1). This framework aims to choose the most suitable stimulation sites based on the projections affected by the PD symptom of interest and the network topological configuration. As large-scale basal ganglia and brainstem models often require biological details, which may not be fully available empirically, here we focus on a general model of excitable dynamics, the discrete three-state SER model [18, 19]. The letters S-E-R denote the basic node behavior of susceptible (S) nodes becoming excited (E) by excited neighbors, then refractory (R), before turning once again susceptible, all in discrete time steps. Such basic excitable models, due to their small parameter space, allow studying exhaustively the effects of neuroanatomical network organization on network global dynamics and activity propagation [20]. One

can observe all the possible emerging dynamical patterns in the network after initializing the graph nodes with all possible initial state conditions. After some time, the dynamics of the network will converge to some repeating patterns, the network attractors. The change in the graph topology, due to projections silenced during DBS, results in a change in the attractor space of the system. This space, in turn, can be converted into a coactivation matrix, as a measure of functional connectivity. Thus, a change in network topology results, via its interpretation through the excitable model, in a change of the functional connectivity of the network.

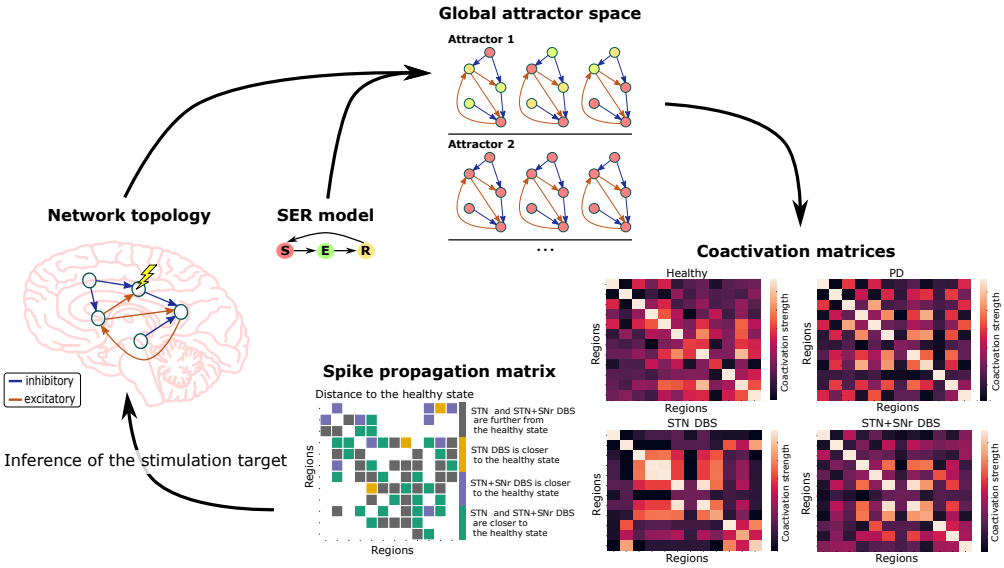

Fig 1. Network-based computational framework to explain the effects of targeting different DBS sites. The SER model is applied to any possible initial conditions in which network nodes can be. This process leads to the emergence of different patterns of excitable dynamics, the network attractors. There are two types of attractors the system can be in: a limit cycle or a fixed point. During a limit cycle, the system repetitively goes through a set of S - susceptible, E - excited, and R - refractory states (attractor 1). By contrast, in the fixed point, all of the network nodes remain in the S state (attractor 2). The attractor space constitutes the coactivation and spike propagation matrices of the system. A change in the network topology due to a DBS target site choice affects the coactivation and spike propagation matrices. Thus, one can infer a suitable stimulation target from the changes in these matrices.

In this study, we explore the changes in dynamical landscapes emerging from the FoG network via the SER dynamics during the STN and STN+SNr DBS modes. We strive to detect the changes in activity propagation in the MLR leading to alleviation of FoG. We hypothesize a normalization of activity propagation in the MLR due to STN+SNr DBS. A further aim of our work is to introduce a general computational network-based framework helping to elucidate large-scale effects resulting from DBS. The framework is not meant to render realistic neuronal dynamics [20], but rather to extract the essential effects of the topological changes caused by DBS on whole-brain network activity patterns.

Results

To study the changes in emerging dynamics induced by the system's state, we employ the network shown in Fig. 2 B. The network includes the basal ganglia and brainstem regions thought to be responsible for FoG episode generation. The FoG network can be in the healthy, PD, STN DBS, and STN+SNr DBS configurations. The PD configuration is obtained from the healthy configuration by setting the weights of the edges originating from the SNc to 0. The same is done for the STN DBS and STN+SNr DBS configurations based on the PD state, by setting the weights of the edges originating from STN, or both STN and SNr, to 0. In the following sections, we first compare the network's topological properties in healthy and PD configurations, then assess the emerging dynamical patterns and corresponding coactivation matrices. Finally, we analyze the activity propagation in different FoG network configurations. Further details can be found in the Materials and methods section.

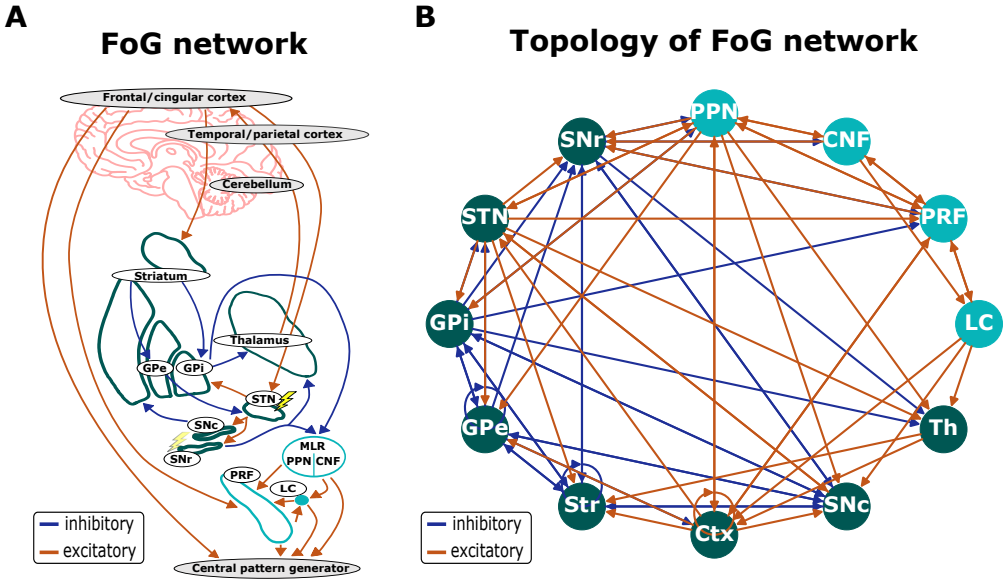

Fig 2. FoG network schematics. A Simplified schematic of the signal flow involved in gait generation and posture control. Lightning symbols indicate potential DBS targets. **B** Graph representation of the FoG network. Inhibitory and excitatory synaptic connections are shown as blue and red arrows, respectively. The basal ganglia regions are shown in green, whereas the brainstem regions are in turquoise. Abbreviations: Ctx - cortex, SNc - substantia nigra pars compacta, striatum, GPi - globus pallidus pars interna, GPe - globus pallidus pars externa, STN - subthalamic nucleus, Th - thalamus, SNr - substantia nigra pars reticulata, MLR - mesencephalic locomotor region, PPN - pedunculopontine nucleus, PRF - pontine reticular formation, CNF - cuneiform nucleus, LC - locus coeruleus.

Topological properties of healthy, PD and stimulated networks

There are changes in the dynamics of the network which could be inferred solely from the changes in the network topology. We assessed graph theoretical measures in the healthy and PD network configurations, to identify if there are topological properties of the FoG network configuration which can promote pathological PD dynamics. The reasoning behind the choice of the graph theoretical measures can be found in the Materials and methods section.

One aspect of the topological differences between the healthy and the PD configurations is a change in the betweenness centrality. In our case, major betweenness centrality changes were observed for SNc, SNr, cortex, and PPN nodes of the graph (Fig. 3 A). The SNc and SNr betweenness centralities drop by 0.04 and 0.02, respectively, upon a change from the healthy to the PD topology. The PPN and cortex betweenness centralities rise by 0.01 and 0.02, respectively, in the PD state compared to the healthy state. While the drop in the SNc betweenness centrality is expected (for details, see the Materials and methods section), the changes in the betweenness centrality of PPN, cortex, and SNr nodes might point to the pathological activity of the brainstem circuits leading to the FoG episodes.

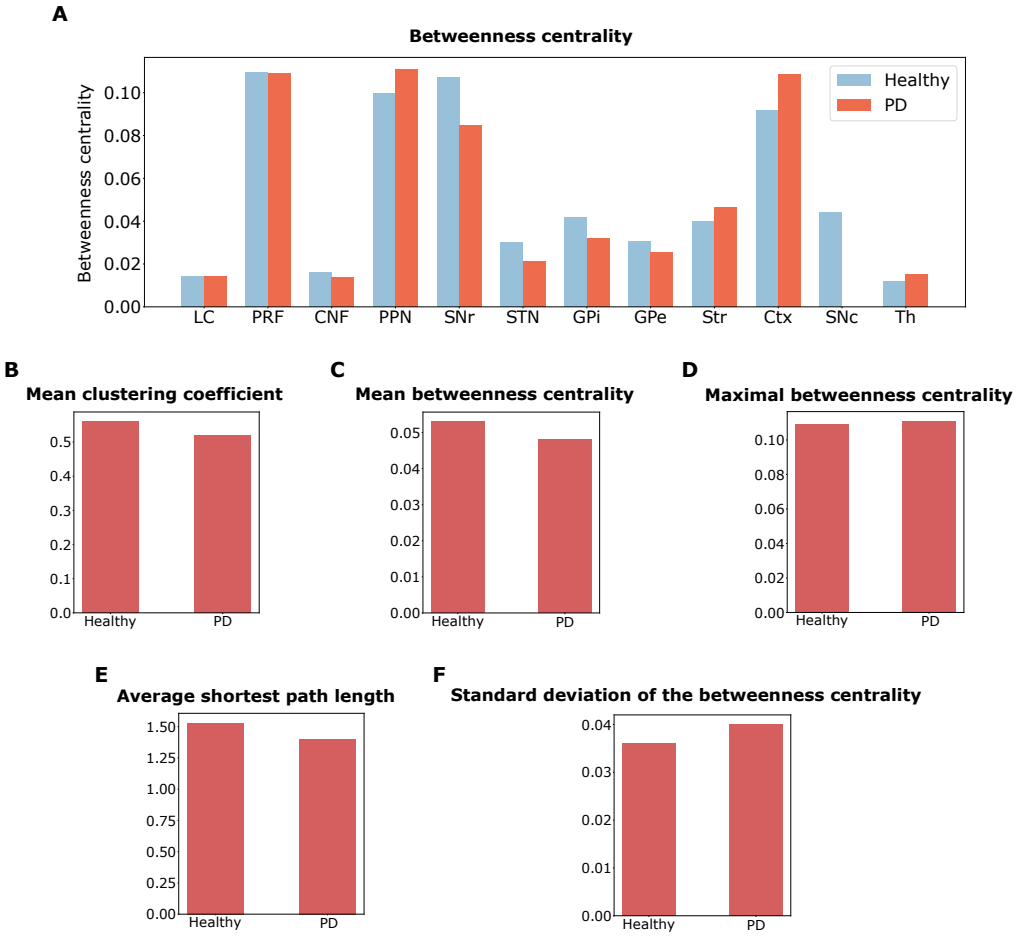

Fig 3. Summary of the graph theoretical measures for the healthy and PD FoG network configurations. A Betweenness centrality sorted by nodes. **B** Mean clustering coefficient. **C** Mean betweenness centrality. **D** Maximal betweenness centrality. **E** Average shortest path length. **F** Standard deviation of the betweenness centrality.

Another aspect of the changes in the network topology, which subsequently defines the dynamics of the system, are the changes leading to the synchronization of the nodal activities. This is of interest, as PD is known to promote abnormal synchronous activity of the basal ganglia nuclei [21, 22]. The graph theoretical measures thought to be responsible for the nodal synchronization for the topology of the FoG network in the healthy and the PD state are assessed in Fig. 3.

For the FoG network, the mean clustering coefficient, mean betweenness centrality,

and average shortest path length decrease between the healthy and the PD configurations, while maximal betweenness centrality and standard deviation of the betweenness centrality increase (Fig. 3). These changes, despite their intricate nature and interactions, usually promote synchronization.

The changes in the modularity were also assessed for the healthy and PD FoG network configurations. We observe that the PD state leads to a larger number of communities in the graph (Fig. 4). This increase in modularity could be viewed as a pathological fragmentation of the FoG network in the PD configuration, which might be interpreted as a disconnection syndrome similar to [23].

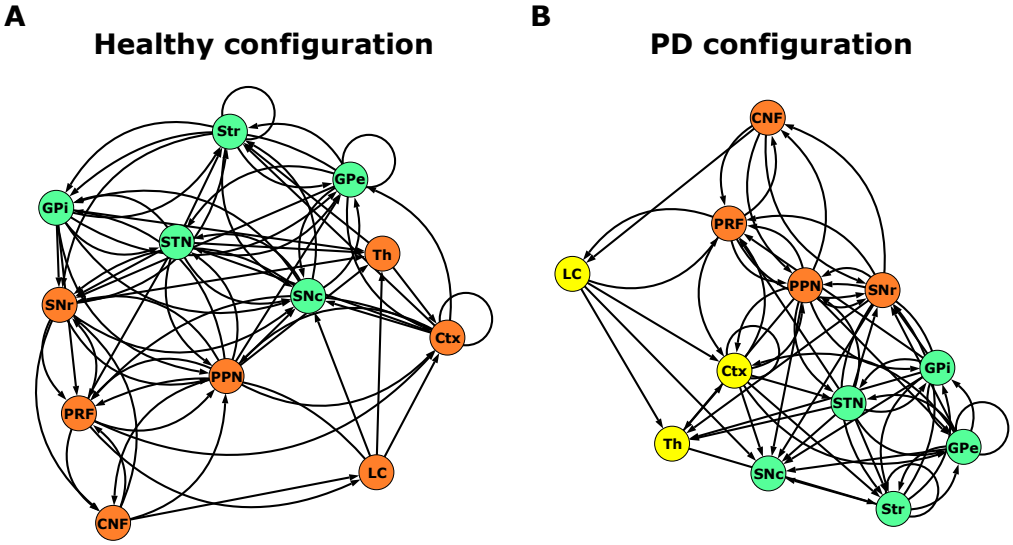

Fig 4. Identified communities for the FoG network. A Healthy configuration. Two major communities are detected (in green and orange). The green community includes almost all the basal ganglia nuclei except for the SNr. **B** PD configuration. Three major communities are detected (in green, orange, and yellow). The green community includes almost all the basal ganglia nuclei except for the SNr. The orange community includes the brainstem regions, except for the LC. The yellow community includes the cortico-thalamic loop and the LC.

Thus, the PD FoG network topology appears to promote synchronized dynamics while having a more disconnected structure.

Emerging dynamical patterns

Emerging dynamical landscapes for the healthy, PD, and DBS configurations of the FoG network are derived from the excitation patterns of the deterministic SER model (see Materials and methods). These patterns regarding the FoG network configurations are summarized in Table 1. The numbers of fixed points and period-3 limit cycles largely vary depending on the network configuration. It should be noted that for the configurations with the smaller number of period-3 limit cycles (healthy and STN DBS configurations), the number of unique period-3 limit cycles is also smaller.

An example of an emerging dynamical landscape for the healthy network configuration is shown in Fig. 5. It is noticeable that the largest proportion of all initial conditions converges to a fixed point (Fig. 5 right inset, Table 1). In a fixed point, all the network nodes are constantly in the susceptible state. All the other initial conditions converge to 31 different period-3 limit cycles. The limit cycle with the largest basin of attraction is shown in the left inset of Fig. 5. Every node in the graph

Table 1. A summary of dynamical landscapes for the different FoG network configurations

	Healthy	**PD**	**STN DBS**	**STN+SNr DBS**
Number of fixed points	452600 (85%)	373074 (70%)	476559 (90%)	284931 (54%)
Number of period-3 limit cycles	78841 (15%)	158367 (30%)	54882 (10%)	246510 (46%)
Number of unique limit cycles	31	56	8	53
Largest limit cycle in a limit cycle space	15%	35%	31%	15%

The numbers of fixed points and period-3 limit cycles are also shown in percentages with respect to the total number of initial conditions ($3^{12} = 531.441$). The last row shows the fraction of the limit cycle with the largest basin of attraction in a limit cycle space in percentages.

repeatedly goes through a loop of S, E, and R states. The coactivation pattern of nodes is different for different period-3 limit cycles. Additionally, Table 1 shows that the period-3 limit cycle with the largest basin of attraction constitutes more than 30% of the limit cycle space for the PD and STN DBS network configurations.

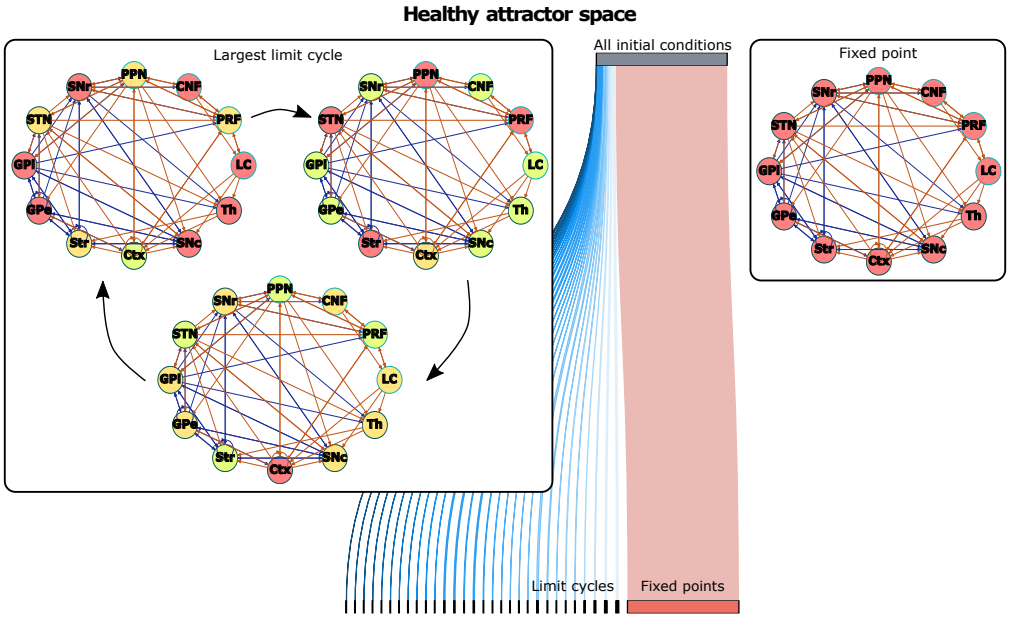

Fig 5. Emerging dynamical landscape for healthy network configuration. For the different combinations of the initial conditions of the SER dynamics, the healthy network topology converges to fixed points (right inset) and period-3 limit cycles (the largest one is shown in the left inset).

From an additional analysis, we note that for the 42% of the limit cycles in the healthy network configuration, the striatum is always in a susceptible state S. By contrast, this is only the case for 4% of the PD limit cycles. During the STN DBS and the STN+SNr DBS, the proportion rises back to 17%.

To compare the emerged limit cycles for different topological configurations of the network, we utilized Venn diagrams (Fig. 6).

We created PD and DBS topological configurations of the FoG network by changing the weights of all edges coming from a certain node to 0 (see section Materials and methods for further details). In a deterministic SER model, this approach is equivalent to an external control exerted over the healthy, or, in the DBS case, PD FoG network configuration [24]. When an external control is exerted over a network, the basin of

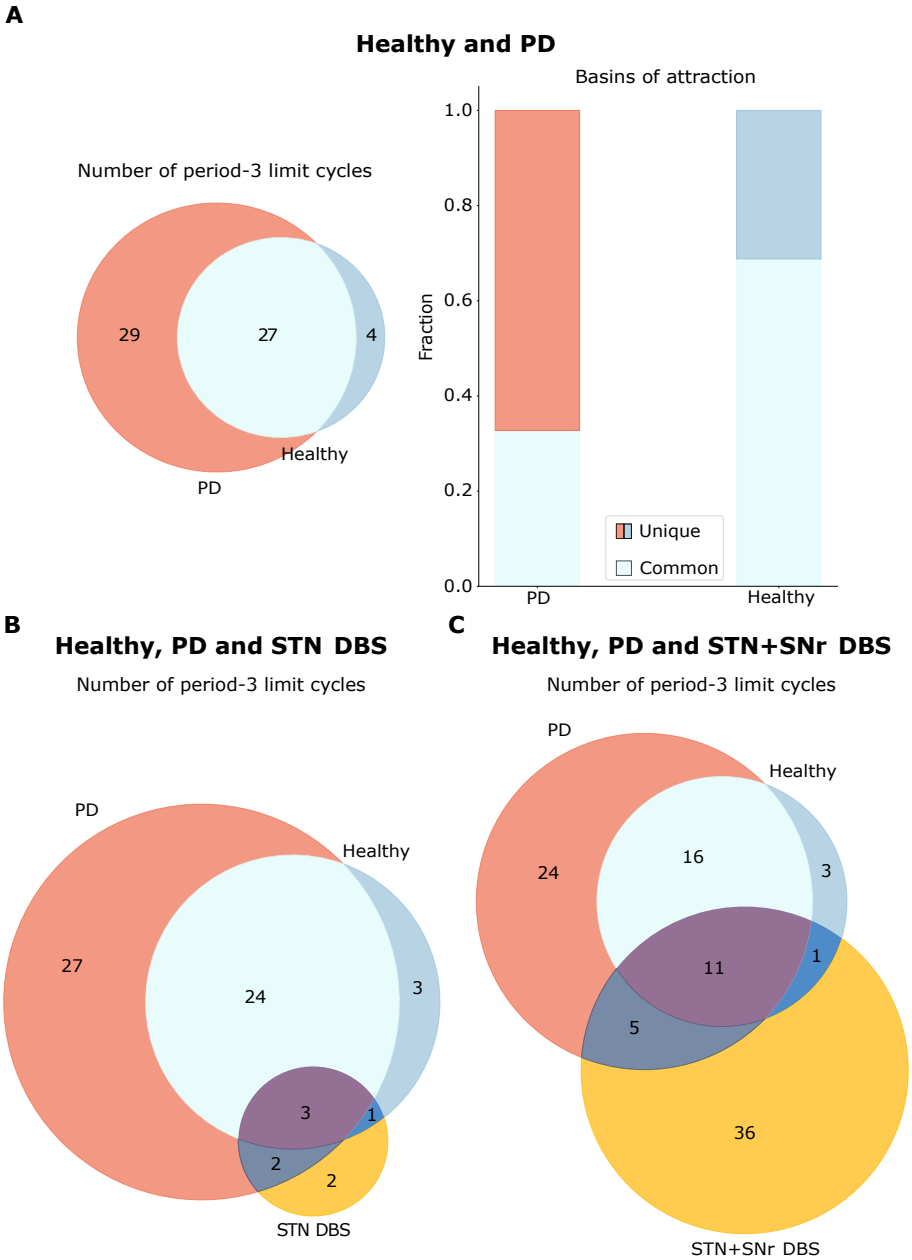

Fig 6. Healthy, PD, and DBS limit cycle spaces. Limit cycles unique to the healthy, PD, and DBS configurations are shown in blue, red, and yellow, respectively. Limit cycles, which are similar in the healthy and PD configurations, are shown in light blue. Limit cycles, which are similar in the DBS and PD configurations, are shown in gray. Limit cycles, similar in the DBS and healthy configurations, are shown in dark blue. Limit cycles, which are similar across all configurations, are shown in purple. The numbers inside the circles are the numbers of the limit cycles of an aforementioned type. **A** Healthy and PD configurations. On the right side, the basins of attractions are compared across configurations, with the fraction of the basin size to the number of limit cycles depicted along the Y-axis. **B** The STN DBS configuration. **C** The STN+SNr DBS configuration.

original attractors of the network can change, or new attractors can emerge [25]. Thus, a successful intervention, in our case DBS, can be viewed as the steering of the PD system towards an original healthy attractor space.

The healthy and the PD attractor spaces are compared in Fig. 6 A. It can be seen that during the exerted external control process of moving from the healthy to the PD configuration, new attractors have emerged (red attractors in Fig. 6 A). In addition, the basins of attraction of the original attractors have changed (right panel in Fig. 6 A). Moreover, it is noticeable that healthy and PD configurations share several common limit cycles. An additional analysis showed that the limit cycle with the largest basins of attraction in the PD configuration does not appear in the healthy configuration. From the right panel in Fig. 6 A, one can see that the fraction of the basins of attraction of the unique healthy limit cycles is much smaller than the fraction of the ones that appear in both the healthy and the PD configurations. Thus, for DBS, it is less likely to steer the system back towards its unique healthy attractors than to the attractors shared in common between the configurations, or to some new attractors.

In Fig. 6 B, the healthy, the PD, and the STN DBS limit cycle spaces are compared. One can see that there are only two new attractors emerging from the PD attractor space (in yellow). At the same time, the dynamical landscape of the STN DBS network includes one of the healthy attractors, which are not the same as for the PD state (in dark blue). This attractor has the striatum node always in a state S, which again points out the quiescence of the striatal neurons in the healthy conditions [26]. From an additional analysis, we found that in the STN DBS configuration the system has moved away from the largest limit cycle in the PD configuration.

In Fig. 6 C the healthy, the PD, and the STN+SNr DBS limit cycle spaces are compared. One can see that, in contrast to the STN DBS, there are many new attractors emerging from the PD space (in yellow). At the same time, the dynamical landscape of the STN+SNr DBS network includes one unique, healthy attractor (in dark blue). This is the same attractor as in Fig. 6 B. However, the whole system has rather moved into the new dynamical space, as there are 36 new limit cycles, which constitute 66% of all the limit cycles in the STN+SNr DBS attractor space. From an additional analysis, we found that in the STN+SNr DBS configuration, the network has also moved away from the largest limit cycle in the PD configuration.

Coactivation matrices

The coactivation matrices for the healthy, the PD, and the DBS configurations are shown in Fig. 7. The details behind the coactivation matrices implementation can be found in the Materials and methods section.

The coactivation matrices in the healthy and the PD states differ (Fig. 7 A, B). The pattern of activity in the healthy matrix appears to be smooth, whereas the pattern is more checkerboard in the PD coactivation matrix. Fig. 7 E shows how close the DBS coactivation matrices are to the healthy one. We checked it by using the 1-norm distance. Indeed, the STN+SNr DBS coactivation matrix is more similar to the healthy state coactivation matrix relative to the PD configuration. On the other hand, the STN DBS coactivation matrix does not exhibit this behavior.

Activity propagation

There is a hypothesis that the normalization of excitatory signals propagation in brainstem regions might be the reason for successful STN+SNr DBS during FoG [27]. Thus, we assessed not only the general coactivation activity of the regions, but also the activity-based projections between them. To this end, we used the activity propagation

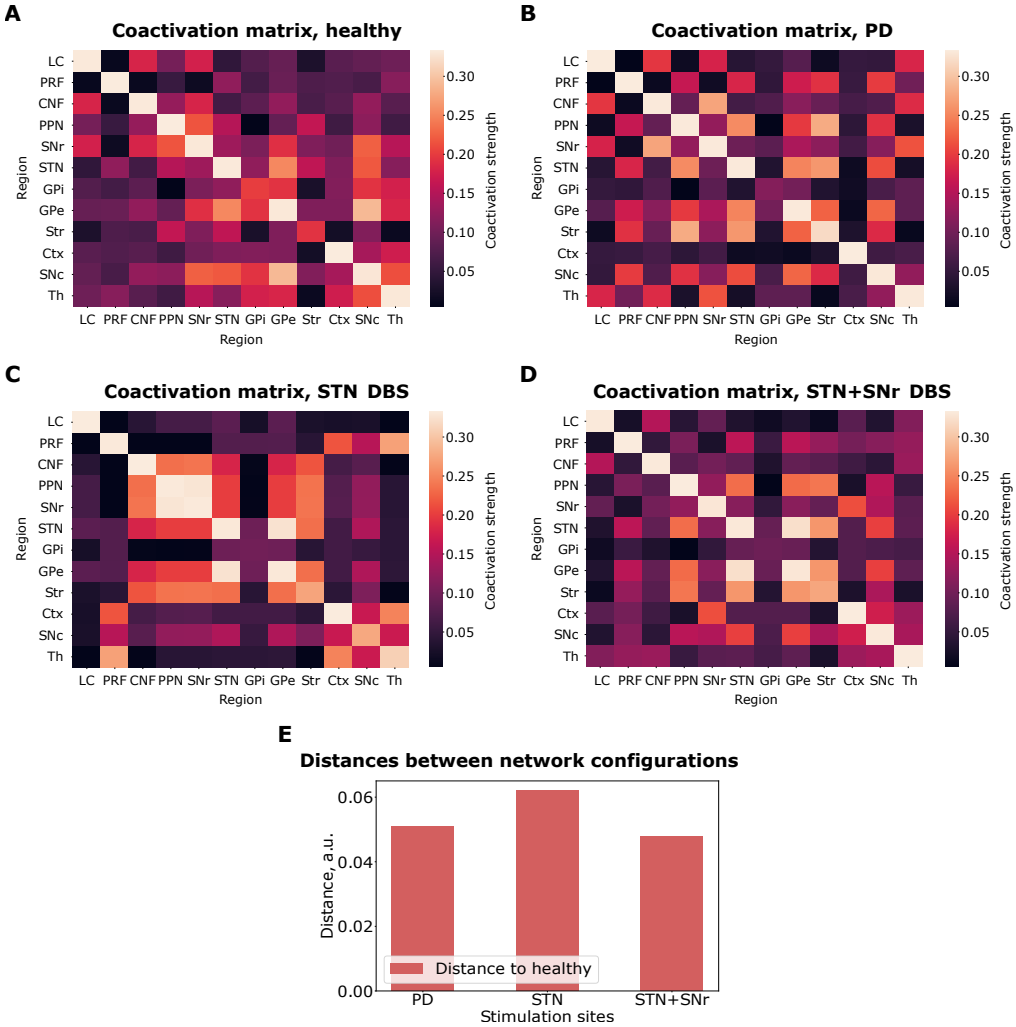

Fig 7. Coactivation matrices. **A** The healthy configuration. **B** The PD configuration. **C** The STN DBS configuration. **D** The STN+SNr DBS configuration. **E** 1-norm distances between the coactivation matrices from the PD, STN DBS and STN+SNr DBS to the healthy state.

matrix (Fig. 8). The details behind its implementation can be found in the Materials and methods section.

Fig. 8 shows a general normalization of the spike flow during both of the DBS configurations (more green, yellow, and purple squares overall). However, it is also noticeable that for the normalization of excitatory propagation along the brainstem projections, the STN+SNr DBS is exclusively effective (purple squares for the LC-PRF, PRF-LC, PRF-PPN, LC-Ctx projections). Fig. 8 also reveals that STN DBS is more beneficial for specific projections (yellow squares), which might indicate the nodes of concern for the STN+SNr DBS configuration.

Discussion

In this study, we present a new network-based computational framework to uncover dynamical landscapes and activity propagation in the brain networks relevant for

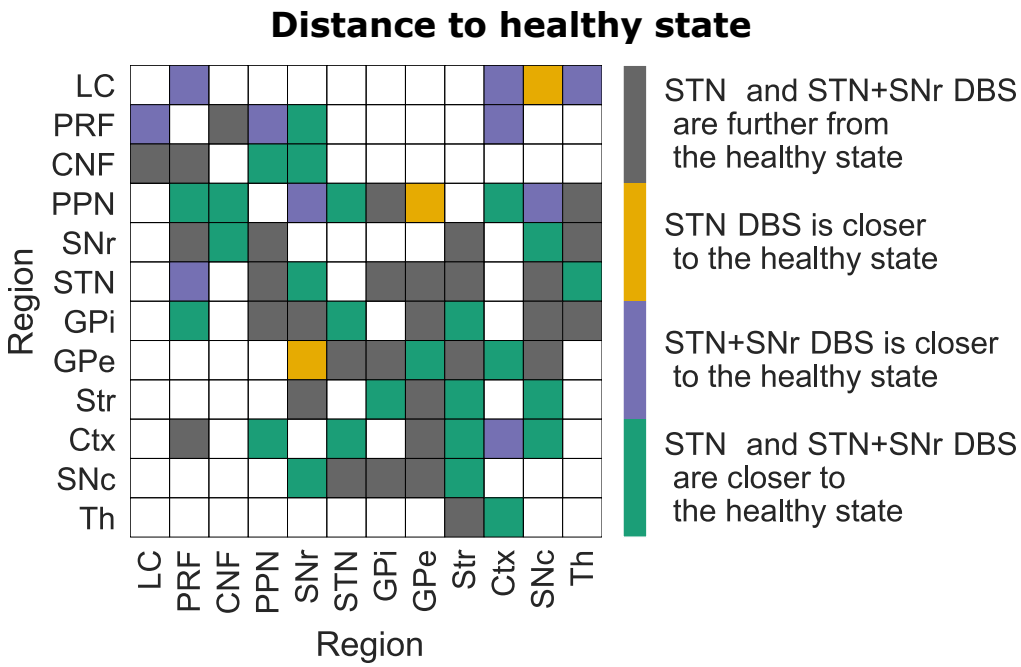

Fig 8. Spike propagation flow normalization. Projection source regions are shown along the Y-axis, while projection targets are shown along the X-axis. The projections are color-coded based on how far they are from the healthy state under different DBS configurations.

understanding symptoms of Parkinson's disease. The framework aims to discover the most suitable DBS targets depending on the projections of importance. In the context of FoG in PD, we found that STN+SNr DBS outperforms the standard STN DBS in terms of activity propagation normalization in the brainstem regions. Activity propagation flow is closer to the healthy state propagation flow in LC-PRF, PRF-LC, PRF-PPN, and LC-Ctx projections for the STN+SNr DBS. This result confirms previous clinical studies which found that STN+SNr DBS outperforms STN DBS in the context of FoG symptoms [8–10]. According to the hypothesis in [16], SNr stimulation leads to temporal regularization of gait and normalization of the output to the MLR and brainstem projections signaling, which is corroborated by the present results.

To achieve this result, we first checked topological properties of the FoG network in the healthy and PD configurations. We studied graph theoretical measures and assessed the corresponding FoG network synchrony in the PD configuration (Fig. 3). The PD FoG network topology likely promotes synchronized activity, which additionally validates the connections in the FoG network (Fig. 2 B). Synchronicity is arguably not the most straightforward measure for assessing whether the graph network is closer to the PD state or not. There are also small-worldness [28], global efficiency, calculation of minimum spanning trees, and other approaches [29]. However, when taken alone, these measures typically lead to inconsistent results across the literature [29, 30] or are inefficient in the case of signed [31] or directed graphs. As the directionality of the graph is an essential biological parameter in our modeling framework, we needed to take this property into account. In turn, the network being a signed graph is was needed for the utilized SER model and provided the framework for its computational power. That is why we assessed the network synchronicity, which is also an essential biological property of PD [21, 22].

Thereafter, we studied dynamical landscapes of the FoG network in healthy, PD,

STN DBS, and STN+SNr DBS configurations using the discrete excitable SER model. The modeling approach might seem simplistic, although it exhibits the most important properties of the three-state excitatory cycle of neural elements. At the same time, the amount of biological realism required for an optimal spiking model to capture the PD dynamics is an open question. Our network-based SER framework is not intended to render realistic neuronal firing patterns. Nevertheless, it captures essential aspects of the PD and DBS dynamics. Analysis of attractors with the largest basins of attraction (Table 1) reveals that for the PD FoG network configuration, the largest basin of attraction constitutes 35% of the limit cycle space. This is a large increase compared to the healthy configuration (15% of limit cycle space). This increase might be interpreted as a sign of abnormal synchrony within the basal ganglia nuclei during PD [32]. During the STN DBS, the amount of limit cycle space taken up by the attractor with the largest basin of attraction does not fall significantly (31%). This might indicate the topological change leading to STN DBS regularization of the firing patterns in basal ganglia by their entrainment [33]. Indeed, the activities in basal ganglia nuclei are highly correlated with one another for the attractor with the largest basin of attraction in the STN DBS configuration. Additionally, there is a change in activity of the striatal neurons. The number of striatal neurons in a susceptible state S decreases in the PD topology, when compared to the healthy topology. Striatal neurons are known to be nearly quiescent in the healthy condition, while their firing rates rise to about 17 Hz during the PD [26]. However, the human recordings by Moll et al., 2015 [34] suggest the PD value to be $2-5$ Hz. During DBS, the firing rate of striatal neurons tends to go back to the healthy range independently of the chosen DBS target.

The network-based SER framework allows exhaustive assessment and comparison of the emerging dynamical landscapes (Fig. 6). This approach helps to answer one of the long-standing questions in DBS research, namely the working mechanism behind it. We can see that the system moves away from the most prominent attractors in the PD configuration for both DBS conditions. Although moving towards the healthy configuration attractors is less likely (Fig. 6 A, right panel), both DBS attractor spaces incorporate one unique healthy attractor. Otherwise, the system for the DBS exhibits a trend to move away to a new attractor space (yellow parts of Fig. 6 B, C). This observation is in accordance with the conclusions by Wichmann and DeLong [32]. They state that the system for the DBS reaches a new equilibrium, rather than induces restoration of normal basal ganglia function. This new equilibrium releases the downstream MLR areas from pathological basal ganglia output.

We continued to study the new equilibrium DBS states by exploring the coactivation matrices and spike propagation flow in the FoG network. The coactivation matrices revealed that combined STN+SNr DBS is closer to the healthy state in terms of functional connectivity (Fig. 7). Furthermore, the checkerboard pattern of activations in the PD coactivation matrix reaffirmed the fragmentation of the FoG network into more communities, similar to the results in Fig. 3. The spike propagation flow normalization in the MLR (Fig. 8) exclusive to the STN+SNr DBS reaffirms the hypothesis on its working mechanism by [16]. Additionally, it captures the normalization of the cortico-thalamic connectivity towards the healthy controls for DBS [35].

The healthy FoG network topological configuration governs the resulting dynamical output, as network topology is the most influential parameter in the SER model. In the present study we used the topology described in Fig. 2 B. The initial choice of this signed graph heavily affects the observed dynamical patterns. We motivated this network choice by comparing the healthy FoG network configuration with a mesoscale connectome from [36] (S1 Fig). Specifically, we compared the weights of the edges from the Allen brain atlas data in [36] with the corresponding weights of the edges in the healthy FoG network in S1 Fig. It can be seen that the regions without edge

connections in the FoG network correspond to the group of edges with the weights clustered around 0 (orange violin plot). Otherwise, strong inhibitory or excitatory connections cluster around -1 and 1 in the FoG network, respectively, as expected. There are no edges with large weights in [36], which would correspond to a 0 weight in the FoG network. Thus, the healthy FoG network configuration in Fig. 2 B depicts the most significant connections in the Allen brain atlas connectome [36], which supports the reliability of the chosen topology.

Overall, we propose a practical computational framework that simultaneously captures the essential aspects of PD and DBS, explores the new STN+SNr DBS approach and confirms its efficiency in the context of FoG.

Conclusion

Selecting the best therapeutic strategy for a specific symptom in PD can be burdensome. In this study, we propose a straightforward network-based computational framework to determine the most suitable DBS target for treating FoG. This approach is based on a discrete SER model and requires only preliminary knowledge of the cortico-subcortical network topology. We also showed that STN+SNr DBS is more beneficial for patients with FoG due to the normalization of the spike propagation flow in the MLR, which confirms our initial hypothesis. In the future, we aim to explore additional DBS targets and network regions, specifically the limbic system, to check the influence of STN+SNr DBS on mood and anxiety.

Materials and methods

The FoG network

The freezing of gait network (Fig. 2 B) was used to compare possible network effects induced by STN DBS and STN+SNr DBS. These effects were then used to identify the possible working mechanisms behind DBS and to infer a suitable stimulation mode for FoG. The network consists of the basal ganglia, the motor cortex, the thalamus, the pedunculopontine nucleus, the pontine reticular formation, the cuneiform nucleus, and the locus coeruleus. The choice of the network regions and connections was based on an analysis of the anatomical literature [37–39]. A schematic for locomotion control [37] was a primary resource used for the construction of the network. The brainstem circuitry was also partially taken from the Mouse Brain Connectivity Atlas provided by Allen Institute [36, 40] in order to expand the network.

The FoG network can be represented as a directed signed graph. The nodes of this graph are the brain regions which are involved in the FoG network. The weights of the edges are set to $+1$ or -1 in the case of the excitatory and inhibitory synaptic projections, respectively. To compare the possible effects induced by STN or STN+SNr DBS on the FoG network, we explored their dynamics in four possible *configurations*: healthy, PD, STN DBS, and STN+SNr DBS. To implement the PD configuration, we set the weights of all edges originating from the SNc node to 0. This approach was chosen because Parkinson's disease is characterized by the degeneration of dopaminergic neurons in SNc, which results in a dopamine depletion in the efferent targets of the SNc [41]. In our model, this degeneration was taken to be equivalent to the disconnection of the SNc from the FoG network. The DBS configurations were created from the PD by setting the weights of all the edges originating from the stimulation target node to 0. This approach is in accordance with the virtual lesion hypothesis being the working mechanism behind the DBS [17]. The hypothesis is based on the similarity between the effects observed after surgical lesions of the brain regions and

their high-frequency DBS. According to this idea, DBS is thought to function via inhibition of the neurons in the vicinity of the stimulating electrode. In our model, this phenomenon was taken to be equivalent to the disconnection of the DBS target region. Thus, in the case of STN DBS, the weights of all the edges originating from the STN node were set to 0. During the combined STN+SNr DBS, the weights of the edges originating from both the STN node and the SNr node were set to 0.

Graph theoretical measures

Changes in network topology can affect the resulting network dynamics [42–44]. The dynamics can become more or less synchronized among various network nodes upon the changes in graph theoretical measures, which assess different aspects of network topology. Here we focus on the measures often thought to affect node synchronization [45–47]: clustering coefficient, mean betweenness centrality, maximal betweenness centrality, and average shortest path length.

Clustering coefficient corresponds to the density of connections between a node's neighbors [42]. When the clustering coefficient is high, the node is densely connected with its neighbors and forms a local cluster. The mean clustering coefficient represents the average of clustering coefficients across all the graph nodes. A decrease in the mean clustering coefficient usually promotes synchronization [47].

Betweenness centrality reflects the node's influence on the activity flow in the graph [48]. It is based on the node's ability to participate in the network's shortest path. This participation results in the node controlling a network's activity [42]. The maximal betweenness centrality of the graph corresponds to the largest betweenness centrality among the nodes, whereas the mean betweenness centrality corresponds to the mean of the betweenness centrality across nodes [45]. For the betweenness centrality measures, the relationship with synchronization is complex. Synchronization tends to increase with the maximum betweenness centrality [47] while in contrast it decreases with the mean betweenness centrality [45]. However, there are more complex cases where one should observe the heterogeneity of the betweenness centrality of the network [46, 47]. We measure heterogeneity of the betweenness centrality by assessing its standard deviation across nodes. More homogeneous distributions of centralities tend to promote more synchronization [46]. On the other hand, the authors in [47] report the opposite, indicating that this measure cannot solely assess synchronization in complex networks.

Average shortest path length relates to the efficiency of the information processing in a network and corresponds to the average shortest path length between every pair of nodes in the graph [47]. Usually, a decrease in the average shortest path length promotes synchronization [45, 47].

Modularity assesses the extent to which a network can be segregated into connected neighborhood [42]. Here it was evaluated using the Leiden community detection method for directed and weighted graphs [49].

The SER model

We studied all possible dynamical patterns which emerge in the healthy, PD, and DBS FoG networks. Thus, for computational effort, a minimal excitable dynamical system, a discrete excitable SER model [18, 19] was used. In the SER model, the S stands for susceptible, E excited, and R refractory states. In the deterministic version of the model, the node goes through the aforementioned states. If the node is in a susceptible state S and if the sum of the weights of the edges originating from excited neighbouring nodes and converging on the target note is larger than 0, then in the following discrete time step, this node will become excited (E). From the E state, the node will always go

to a refractory state R. In turn, from the R state, the node will always go to the state S in the following discrete time step.

We applied the SER model over all possible initial conditions of the FoG network for the healthy, PD, and DBS network configurations to explore and compare emerging dynamical patterns. At the beginning, every node of the FoG network could be in one of the states: S, E, or R. After considering all possible combinations of these initial conditions, every possible dynamical pattern which can emerge in the FoG network for a certain topological configuration was explored. After that, the dynamical landscapes were compared between the healthy, PD, STN DBS, and STN+SNr DBS FoG network configurations.

As the SER model is a three-state model, there are 3^n possible patterns of activity in a network with n nodes. These patterns of activity represent the *states* of the network. Thus, the network dynamics can be represented as a time series of the states. As the amount of the states is finite for a system with a finite number of nodes, the dynamics of the network eventually converges to one of two types of behavior, the *attractors*. The first type of attractor is a *fixed point*. The system reaches a fixed point after some transient time when all nodes in the network remain in the state S. The other attractor type is a *limit cycle*. In this case, all the nodes in the network will go through a series of the S, E, and R states with a period of $3k$, where $k \in N$. Attractors could be compared via their *basin of attraction*, which is a set of initial states that converge onto a particular attractor [24]. Thus, to compare the dynamical landscapes in the various FoG network states, we compared the emerging attractors and their basins of attraction for different FoG network configurations and the SER dynamics after the time $T = 100$ with the transient time $t = 40$.

Additionally, we studied coactivation and activity propagation patterns of the network in different configurations. Coactivation matrices were obtained from the time series of the network states by summing up simultaneously occurring spiking events (E states).

To calculate the activity propagation flow in the FoG network under different topological configurations, we calculate 1-norm distances between coactivation matrices corresponding to the FoG network projections. We assessed the activity propagation flow differently depending on whether the projection in the FoG network was excitatory or inhibitory.

To study excitatory projections, we used the shifted version of the coactivation matrices (Fig. 9 A). It is obtained by shifting the activity of the projection target region one time step further from the activity source region. This way, if the excitatory state E co-occurs in the projection target and the source region, it means that the excitation of the target follows the excitation of the source. In our model, this was the case for the excitatory projections.

To assess activity propagation flow along the inhibitory projections of the FoG network, we used the usual coactivation matrices (Fig. 9 B). If the excitatory state E occurred simultaneously in the projection target and the projection source region, it meant that the excitation of the source was followed by the target in the refractory state R on the next time step. This would be true only after the transient time when the system has reached its stable dynamical pattern. In our model, the excitation of the source followed by the target region entering the refractory state wwas equivalent to inhibition. Thus, we utilized the coactivation matrices to assess the spike propagation along the inhibitory projections.

After obtaining the shifted and synchronous coactivation matrices, we calculated 1-norm distances between them for each FoG network region pair and color-coded them based on whether the distance was closer to the healthy or the PD state under different DBS configurations. The obtained matrix was masked to depict only inhibitory and

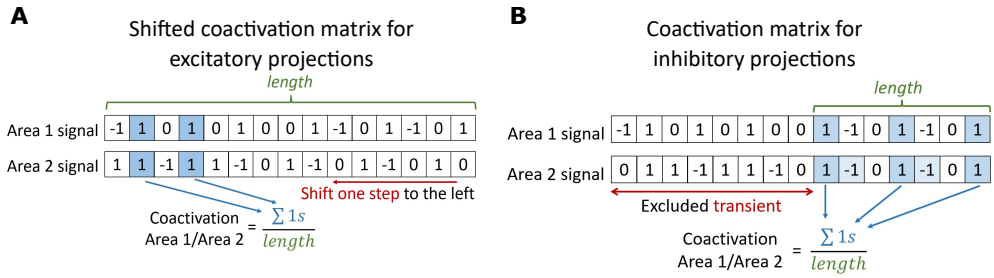

Fig 9. Mechanism to assess spike propagation flow. A Shifted coactivation matrix for excitatory projections. After the shift of one signal to the left, the co-occuring E states are calculated. **B** Coactivation matrix for inhibitory projections. After exclusion of transient time t, the co-occuring E states are calculated.

excitatory projections which exist in the FoG network (Fig. 8).

Supporting information

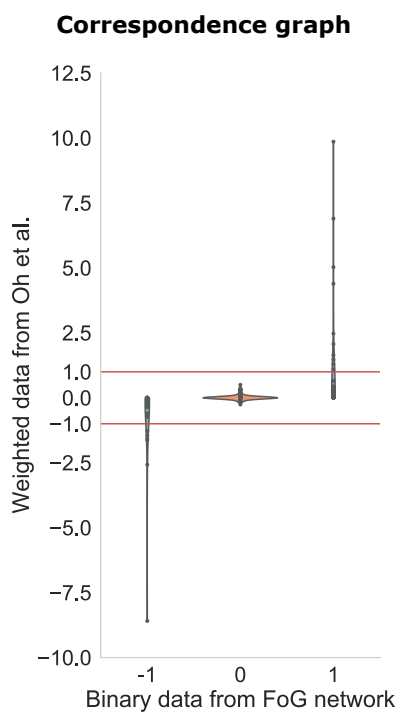

S1 Fig. Connectome comparison. The edge weights from [36] (Y-axis) are grouped along the binary weights of the corresponding edges used in healthy FoG network configuration (X-axis). The red lines show 1 and −1 weights borders.

Acknowledgments

MP, AM, CCH, MPN, AG, CG were funded by the Deutsche Forschungsgemeinschaft (DFG, German Research Foundation) - SFB 936 - Project-ID 178316478-A1/C1/C8/Z3.

References

1. Postuma RB, Berg D, Stern M, Poewe W, Olanow CW, Oertel W, et al. MDS clinical diagnostic criteria for Parkinson's disease. Movement disorders. 2015;30(12):1591–1601.

2. Fox SH, Katzenschlager R, Lim SY, Barton B, De Bie RM, Seppi K, et al. International Parkinson and movement disorder society evidence-based medicine review: update on treatments for the motor symptoms of Parkinson's disease. Movement Disorders. 2018;33(8):1248–1266.

3. Deuschl G, Antonini A, Costa J, Śmiłowska K, Berg D, Corvol JC, et al. European Academy of Neurology/Movement Disorder Society-European Section guideline on the treatment of Parkinson's disease: I. Invasive therapies. European Journal of Neurology. 2022;29(9):2580–2595.

4. Deuschl G, Paschen S, Witt K. Clinical outcome of deep brain stimulation for Parkinson's disease. Handbook of clinical neurology. 2013;116:107–128.

5. Pötter-Nerger M, Volkmann J. Deep brain stimulation for gait and postural symptoms in Parkinson's disease. Movement Disorders. 2013;28(11):1609–1615. doi:10.1002/mds.25677.

6. Schlenstedt C, Shalash A, Muthuraman M, Falk D, Witt K, Deuschl G. Effect of high-frequency subthalamic neurostimulation on gait and freezing of gait in Parkinson's disease: a systematic review and meta-analysis. European journal of neurology. 2017;24(1):18–26.

7. Pollak P. Deep brain stimulation for Parkinson's disease–patient selection. Handbook of clinical neurology. 2013;116:97–105.

8. Weiss D, Walach M, Meisner C, Fritz M, Scholten M, Breit S, et al. Nigral stimulation for resistant axial motor impairment in Parkinson's disease? A randomized controlled trial. Brain. 2013;136(7):2098–2108. doi:10.1093/brain/awt122.

9. Horn MA, Gulberti A, Hidding U, Gerloff C, Hamel W, Moll CK, et al. Comparison of Shod and Unshod Gait in Patients With Parkinson's Disease With Subthalamic and Nigral Stimulation. Frontiers in Human Neuroscience. 2022;15:800.

10. Wagner JR, Schaper M, Hamel W, Westphal M, Gerloff C, Engel AK, et al. Combined Subthalamic and Nigral Stimulation Modulates Temporal Gait Coordination and Cortical Gait-Network Activity in Parkinson's Disease. Frontiers in Human Neuroscience. 2022;16. doi:10.3389/fnhum.2022.812954.

11. Ulla M, Thobois S, Llorca PM, Derost P, Lemaire JJ, Chereau-Boudet I, et al. Contact dependent reproducible hypomania induced by deep brain stimulation in Parkinson's disease: Clinical, anatomical and functional imaging study. Journal of Neurology, Neurosurgery and Psychiatry. 2011;82(6):607–614. doi:10.1136/jnnp.2009.199323.

12. Ulla M, Thobois S, Lemaire JJ, Schmitt A, Derost P, Broussolle E, et al. Manic behaviour induced by deep-brain stimulation in Parkinson's disease: Evidence of substantia nigra implication? Journal of Neurology, Neurosurgery and Psychiatry. 2006;77(12):1363–1366. doi:10.1136/jnnp.2006.096628.

13. Blomstedt P, Hariz MI, Lees A, Silberstein P, Limousin P, Yelnik J, et al. Acute severe depression induced by intraoperative stimulation of the substantia nigra: a case report. Parkinsonism & related disorders. 2008;14(3):253–256.

14. McIntyre CC, Hahn PJ. Network perspectives on the mechanisms of deep brain stimulation. Neurobiology of Disease. 2010;38(3):329–337. doi:10.1016/j.nbd.2009.09.022.

15. Moro E, Hamani C, Poon YY, Al-Khairallah T, Dostrovsky JO, Hutchison WD, et al. Unilateral pedunculopontine stimulation improves falls in Parkinson's disease. Brain. 2010;133(1):215–224. doi:10.1093/brain/awp261.

16. Scholten M, Klemt J, Heilbronn M, Plewnia C, Bloem BR, Bunjes F, et al. Effects of subthalamic and nigral stimulation on gait kinematics in Parkinson's disease. Frontiers in Neurology. 2017;8(OCT):1–8. doi:10.3389/fneur.2017.00543.

17. Herrington TM, Cheng JJ, Eskandar EN. Mechanisms of deep brain stimulation. Journal of Neurophysiology. 2016;115(1):19–38. doi:10.1152/jn.00281.2015.

18. Müller-Linow M, Hilgetag CC, Hütt MT. Organization of excitable dynamics in hierarchical biological networks. PLoS Computational Biology. 2008;4(9). doi:10.1371/journal.pcbi.1000190.

19. Messé A, Hütt MT, Hilgetag CC. Toward a theory of coactivation patterns in excitable neural networks. PLoS Computational Biology. 2018;14(4):1–19. doi:10.1371/journal.pcbi.1006084.

20. Garcia G, Lesne A, Hütt MT, Hilgetag C. Building Blocks of Self-Sustained Activity in a Simple Deterministic Model of Excitable Neural Networks. Frontiers in Computational Neuroscience. 2012;6. doi:10.3389/fncom.2012.00050.

21. Magnin M, Morel A, Jeanmonod D. Single-unit analysis of the pallidum, thalamus and subthalamic nucleus in parkinsonian patients. Neuroscience. 2000;96(3):549–564. doi:10.1016/S0306-4522(99)00583-7.

22. Hammond C, Bergman H, Brown P. Pathological synchronization in Parkinson's disease: networks, models and treatments. Trends in neurosciences. 2007;30(7):357–364.

23. Göttlich M, Münte TF, Heldmann M, Kasten M, Hagenah J, Krämer UM. Altered resting state brain networks in Parkinson's disease. PloS one. 2013;8(10):e77336.

24. Borriello E, Daniels BC. The basis of easy controllability in Boolean networks. Nature Communications. 2020;12(2021). doi:10.1038/s41467-021-25533-3.

25. Newby E, Tejeda Zañudo JG, Albert R. Structure-based approach to identifying small sets of driver nodes in biological networks. Chaos: An Interdisciplinary Journal of Nonlinear Science. 2022;32(6):063102.

26. Singh A, Mewes K, Gross RE, DeLong MR, Obeso JA, Papa SM. Human striatal recordings reveal abnormal discharge of projection neurons in Parkinson's disease. Proceedings of the National Academy of Sciences of the United States of America. 2016;113(34):9629–9634. doi:10.1073/pnas.1606792113.

27. Pötter M, Herzog J, Siebner HR, Kopper F, Steigerwald F, Deuschl G, et al. Subthalamic nucleus stimulation modulates audiospinal reactions in Parkinson disease. Neurology. 2008;70(16 PART 2):1445–1451. doi:10.1212/01.wnl.0000310422.49977.ea.

28. Vecchio F, Pappalettera C, Miraglia F, Alù F, Orticoni A, Judica E, et al. Graph Theory on Brain Cortical Sources in Parkinson's Disease: The Analysis of 'Small World'Organization from EEG. Sensors. 2021;21(21):7266.

29. Olde Dubbelink KT, Hillebrand A, Stoffers D, Deijen JB, Twisk JW, Stam CJ, et al. Disrupted brain network topology in Parkinson's disease: a longitudinal magnetoencephalography study. Brain. 2014;137(1):197–207.

30. Mijalkov M, Volpe G, Pereira JB. Directed Brain Connectivity Identifies Widespread Functional Network Abnormalities in Parkinson's Disease. Cerebral Cortex. 2022;32(3):593–607.

31. Bassett DS, Bullmore ET. Small-world brain networks revisited. The Neuroscientist. 2017;23(5):499–516.

32. Wichmann T, DeLong M. Basal ganglia discharge abnormalities in Parkinson's disease. Parkinson's Disease and Related Disorders. 2006; p. 21–25.

33. McConnell GC, So RQ, Hilliard JD, Lopomo P, Grill WM. Effective deep brain stimulation suppresses low-frequency network oscillations in the basal ganglia by regularizing neural firing patterns. Journal of Neuroscience. 2012;32(45):15657–15668.

34. Moll CKE, Hamel W, Engel AK. Neurophysiologisches Monitoring in der funktionellen Neurochirurgie bei Bewegungsstörungen: Intraoperative Mikroelektrodenableitungen. Neurophysiologie-Labor. 2015;37(2):102–129. doi:10.1016/j.neulab.2015.05.001.

35. Horn A, Li N, Dembek TA, Kappel A, Boulay C, Ewert S, et al. Lead-DBS v2: Towards a comprehensive pipeline for deep brain stimulation imaging. NeuroImage. 2019;184(August 2018):293–316. doi:10.1016/j.neuroimage.2018.08.068.

36. Oh SW, Harris JA, Ng L, Winslow B, Cain N, Mihalas S, et al. A mesoscale connectome of the mouse brain. Nature. 2014;508(7495):207–214. doi:10.1038/nature13186.

37. Snijders AH, Takakusaki K, Debu B, Lozano AM, Krishna V, Fasano A, et al. Physiology of Freezing of Gait. Annals of Neurology. 2016;doi:10.1002/ana.24778.

38. Takakusaki K. Functional Neuroanatomy for Posture and Gait Control. Journal of Movement Disorders. 2017;10(1):1–17.

39. Pahapill PA. The pedunculopontine nucleus and Parkinson's disease. Brain. 2000;123(9):1767–1783. doi:10.1093/brain/123.9.1767.

40. Allen Institute for Brain Science (2004). Allen Mouse Brain Connectivity Atlas; 2011. Available from: `mouse.brain-map.org`.

41. Delaville C, de Deurwaerdère P, Benazzouz A. Noradrenaline and Parkinson's disease. Frontiers in Systems Neuroscience. 2011;5(MAY 2011):1–12. doi:10.3389/fnsys.2011.00031.

42. Sporns O. Networks of the Brain. MIT press; 2016.

43. Zhou C, Zemanová L, Zamora-Lopez G, Hilgetag CC, Kurths J. Structure–function relationship in complex brain networks expressed by hierarchical synchronization. New Journal of Physics. 2007;9(6):178.

44. Deco G, Jirsa VK, Robinson PA, Breakspear M, Friston K. The dynamic brain: from spiking neurons to neural masses and cortical fields. PLoS computational biology. 2008;4(8):e1000092.

45. DeLellis P, DiBernardo M, Porfiri M. Achieving consensus and synchronization by adapting the network topology. IFAC Proceedings Volumes. 2011;44(1):1243–1248. doi:10.3182/20110828-6-IT-1002.02383.

46. Belykh I, Hasler M, Lauret M, Nijmeijer H. Synchronization and graph topology. International Journal of Bifurcation and Chaos. 2005;15(11):3423–3433.

47. Arenas A, Díaz-Guilera A, Kurths J, Moreno Y, Zhou C. Synchronization in complex networks. Physics reports. 2008;469(3):93–153.

48. Joyce KE, Laurienti PJ, Burdette JH, Hayasaka S. A new measure of centrality for brain networks. PLoS ONE. 2010;5(8). doi:10.1371/journal.pone.0012200.

49. Traag VA, Waltman L, van Eck NJ. From Louvain to Leiden: guaranteeing well-connected communities. Scientific Reports. 2019;9(1):1–12. doi:10.1038/s41598-019-41695-z.